

Uncovering polar vortex structures by inversion of multiple scattering with a stacked Bloch wave model

Steven E Zeltmann^a, Shang-Lin Hsu^b, Hamish G. Brown^c, Sandhya Susarla^d, Ramamoorthy Ramesh^a, Andrew M Minor^{a,e}, Colin Ophus^e

^a*Department of Materials Science and Engineering, University of California, Berkeley, Berkeley, CA*

^b*Materials Science Division, Lawrence Berkeley National Laboratory, Berkeley, CA*

^c*Ian Holmes Imaging Centre, Bio21 Molecular Science and Biotechnology Institute, University of Melbourne, Victoria, Australia*

^d*School for Engineering of Matter, Transport and Energy, Arizona State University, Tempe, AZ*

^e*National Center for Electron Microscopy, Molecular Foundry, Lawrence Berkeley National Laboratory, Berkeley, CA*

Abstract

Nanobeam electron diffraction can probe local structural properties of complex crystalline materials including phase, orientation, tilt, strain, and polarization. Ideally, each diffraction pattern from a projected area of a few unit cells would produce a clear Bragg diffraction pattern, where the reciprocal lattice vectors can be measured from the spacing of the diffracted spots, and the spot intensities are equal to the square of the structure factor amplitudes. However, many samples are too thick for this simple interpretation of their diffraction patterns, as multiple scattering of the electron beam can produce a highly nonlinear relationship between the spot intensities and the underlying structure. Here, we develop a stacked Bloch wave method to model the diffracted intensities from thick samples with structure that varies along the electron beam. Our method reduces the large parameter space of electron scattering to just a few structural

Email addresses: `steven.zeltmann@berkeley.edu` (Steven E Zeltmann), `cophus@gmail.com` (Colin Ophus)

variables per probe position, making it fast enough to apply to very large fields of view. We apply our method to $\text{SrTiO}_3/\text{PbTiO}_3/\text{SrTiO}_3$ multilayer samples, and successfully disentangle specimen tilt from the mean polarization of the PbTiO_3 layers. We elucidate the structure of complex vortex topologies in the PbTiO_3 layers, demonstrating the promise of our method to extract material properties from thick samples.

Keywords: Scanning transmission electron microscopy, Electron diffraction, Nanobeam electron diffraction, 4D-STEM

1. Introduction

Multiple scattering is often viewed as an unwanted and cumbersome artifact in electron microscopy as it is responsible for confounding effects such as contrast reversals in phase contrast images and electric field maps [1, 2], complex features inside nanobeam diffraction disks that hinder precise strain mapping [3–6], and failure of many super-resolution imaging techniques [7]. Despite this, the rich physics of dynamical diffraction also provides us with the ability to very precisely measure material properties. John Spence pioneered the practice of inverting the dynamical scattering process to retrieve the features of materials, developing numerous algorithms for recovering detailed structural information from electron diffraction patterns [8–11]. Following Spence’s legacy, this contribution follows applies the ideas of dynamical inversion to a large-area four-dimensional scanning transmission electron microscopy dataset.

In a naïve sense, an electric field built in to a thin sample causes a tilt of the electron wave as it propagates through the material. Depending on the optical setup and the length scale of the changes in the field this manifests as an intensity redistribution in a diffraction pattern when using a larger convergence angle [12], or a shift of the diffraction pattern when using a small convergence angle [13, 14]. In materials where the polarization is associated with a structural distortion, the diffracted intensities also change as a result of the change in the lattice electrostatic potential [15]. This is shown schematically in Fig. 1a, which shows a sequence of diffraction patterns simulated at differing polarization for a thin (4 u.c., ≈ 1.6 nm) sample of PbTiO_3 (PTO).

When the sample thickness increases and multiple scattering occurs, however, the changes in the diffraction patterns become far more complex than this description. Deb et al. showed that when diffraction disks overlap, under the weak phase approximation there should be no contrast between opposing pairs of diffraction disks due to polarization; however, anomalous contrast between Friedel pairs arises when multiple scattering pathways are considered [16]. Mahr et al [17] showed that for an interface with an electric field due to a difference in mean inner potentials, dynamical scattering causes the measured electric field to oscillate wildly for most experimental setups, with beam precession providing the only partial remedy. Nguyen et al [18] also observed that when measuring chiral polarization domains via the diffraction intensity changes associated with a structural distortion, the chiral directions flip as a function of thickness. This case is shown schematically in Fig. 1b for sample of PTO that is thick enough (16 u.c., ≈ 6.3 nm) to cause multiple scattering of the electron probe.

Various approaches for reconstructing sample properties or structure under conditions of multiple scattering have been developed that utilize the \mathcal{S} -matrix description of the scattering process [8, 19–22]. In these approaches, the electron scattering process is encapsulated in the “scattering matrix,” an object which contains the information about the material structure and thickness-propagation effects, such that the \mathcal{S} -matrix multiplies with a vector representing the incident electron wave to yield a vector representing the scattered wave [23]. As we will discuss in the theory section below, there is useful correspondence between the entries of the \mathcal{S} -matrix and the properties of the sample, such as its thickness, polarization, or tilt. This correspondence can be used in both the forward direction to simulate diffraction intensities given known structural parameters, as well as in the reverse direction to recover structural parameters from diffraction intensities. Much of the literature on this method is concerned with atomic-resolution reconstruction of the sample potential. Donatelli and Spence demonstrated a method for recovering the sample potential at high resolution from a tilt series of diffraction patterns by iterative inversion of the \mathcal{S} -matrix and without prior knowledge of the sample thickness [8]. Brown and coworkers have developed methods for recovery of the \mathcal{S} -matrix, originally from focal series 4D-STEM data [19, 22] and later extended to a single defocus [21]. Their former method provided some 3-dimensional information about the sample, which they

recovered from the \mathcal{S} -matrix by an optical sectioning approach. Alternatively, when the approximate structure of the material is known, and variation along the beam direction can be ascribed to a small number of parameters, the PRIMES (parameter retrieval and inversion from multiple electron scattering) family of methods can be used to obtain property variation along the beam direction [24–27]. These methods all utilize a stacked \mathcal{S} -matrix model to represent parameter variation along the beam direction, which are refined against test CBED patterns using various numerical optimization schemes. Similarly, Jacob et al used quantitative CBED (QCBED) for the determination of structural information from buried interfaces by modeling of the dynamical scattering [28].

In this work, we analyze a complex sample consisting of multiple distinct layers through the thickness, and use a model of the electron multiple scattering to extract information about the material. The sample, consisting of 16 unit cells of SrTiO_3 (STO), 16 unit cells of PTO, and 16 units cells of STO (total thickness ≈ 19 nm), is shown in Fig 1c. The vortex structures in this material have been previously studied by plan-view and cross section transmission electron microscopy [15, 29] and by x-ray coherent diffractive imaging [30]. These vortex structures offer the promise of creating new electronic states of matter, with structured domains with nanometer-scale domain sizes. Similar to PRIMES, we do not aim to recover the full atomic structure of the material. Instead, we model the scattering matrix using parameters (local tilt and polarization) that represent small perturbations from an *a priori* known average structure of the material, and refine the model to match measured diffraction intensities. Parameterizing the scattering model allows us to choose a small and physically meaningful set of variables to refine against, and by computing gradients of the model semi-analytically we are able to dramatically accelerate the discovery of the model parameters. Because mistilt is specifically included as a parameter of the model, slight deviation from the zone axis configuration does not couple into errors in the other recovered signals. By computing the full scattering matrix we are also able to include all beams present in the experiment, enabling the method to work at high-symmetry orientations. By operating on shallow convergence angle nanobeam diffraction patterns, we are able to approximate the diffraction condition as a plane-wave experiment, enabling us to use a smaller \mathcal{S} -matrix that is faster to compute than CBED-based methods such

as QCBED, at the cost of reduced sensitivity from losing the rich phase contrast information present in a CBED pattern. As a result, our method is sufficiently fast to allow us to perform the parameter matching for each probe position in a four-dimensional scanning transmission electron microscopy (4D-STEM) scan, where a shallow converged electron probe is rastered in a 500×400 pixel grid across the sample surface. We find that an advantage of using this dynamical refinement procedure to obtain the local tilt and polarization is that we are able to robustly disentangle these two signals, which often confound one another when measured using conventional approaches, especially for the multi-layer system we examine.

In the Bloch wave description of electron diffraction, which we utilize in this work, the \mathcal{S} -matrix is computed from the Fourier coefficients of the crystal electrostatic potential, the beam direction, and the sample thickness. Thus, our approach can capture a wide variety of structural distortions, such as polar distortions, subtle phase changes, chemical (dis)ordering, and other atomic rearrangements that do not distort the locations of the reciprocal lattice points. The stacked \mathcal{S} -matrix model is further able to incorporate the thickness and tilt of each layer independently. Properties such as strain that *distort* the (reciprocal) lattice in a continuous manner without substantial change in the Fourier coefficients, or major phase changes that alter the (reciprocal) lattice in an abrupt manner, are not included in this approach as the entries of the \mathcal{S} -matrix cannot be expressed in terms of these parameters.

2. Theory

To compute the dynamical diffraction intensities, we utilize the Bloch wave method, which is fully described in DeGraef [31]. In this method, the electron wave is written as a combination of Bloch states, and thus the Schrödinger equation for the fast electron wave is cast as an eigenvalue/eigenvector decomposition

$$\bar{\mathcal{A}}\mathcal{C} = 2k_n\gamma\mathcal{C}, \quad (1)$$

where the “structure” matrix $\bar{\mathcal{A}}$ is determined by the crystal structure and orientation of the sample, \mathcal{C} is a matrix whose column vectors contain the Bloch wave coefficients, k_n is the normal component of the incident wavevector, and γ relative normal component of each of the Bloch waves.

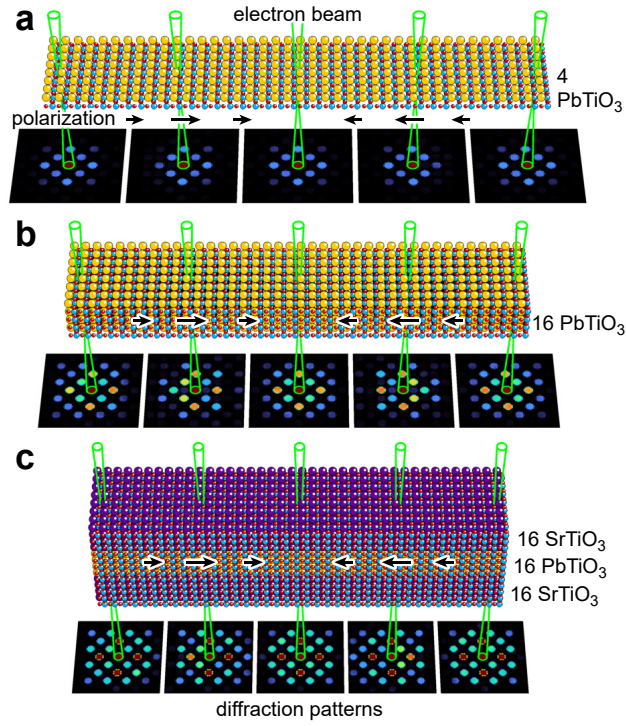


Figure 1: Nanobeam electron diffraction signals from lattices with varying in-plane polarization, indicated by the arrows. Diffraction pattern simulations of (a) thin (4 u.c.) PbTiO_3 , (b) thick (16 u.c.) PbTiO_3 , and (c) multilayer with 16:16:16 unit cells of $\text{SrTiO}_3\text{:PbTiO}_3\text{:SrTiO}_3$. Left to right, the in-plane PbTiO_3 polarization varies smoothly from zero, full left-facing, zero, full right-facing, and zero polarization.

The entries of the structure matrix are given by

$$\bar{\mathcal{A}} = \begin{bmatrix} 0 & U_{-\mathbf{g}} & \cdots & U_{-\mathbf{h}} \\ U_{\mathbf{g}} & 2k_0 s_{\mathbf{g}} & \cdots & U_{\mathbf{g}-\mathbf{h}} \\ \vdots & \vdots & \ddots & \vdots \\ U_{\mathbf{h}} & U_{\mathbf{h}-\mathbf{g}} & \cdots & 2k_0 s_{\mathbf{h}} \end{bmatrix} \quad (2)$$

where $U_{\mathbf{g}-\mathbf{h}}$ is the Fourier component of the sample electrostatic potential corresponding to the scattering vector $\mathbf{g} - \mathbf{h}$ and $s_{\mathbf{g}}$ is the excitation error for the beam \mathbf{g} . The excitation error is given by

$$s_{\mathbf{g}} = \frac{-\mathbf{g} \cdot (2\mathbf{k} + \mathbf{g})}{2|\mathbf{k} + \mathbf{g}| \cos \alpha} \quad (3)$$

where \mathbf{k} is the wavevector of the incident electron beam, and α is the angle between the sample normal and the incident beam direction. To include absorption due to thermal diffuse or inelastic scattering, an imaginary component of the sample potential $U'_{\mathbf{g}}$ is included in the matrix $\bar{\mathcal{A}}$ by adding $iU'_{\mathbf{0}}$ to the diagonal and $iU'_{\mathbf{g}-\mathbf{h}}$ to the off-diagonal. By computing the eigenvalue/eigenvector decomposition of this matrix, we obtain the Bloch wave coefficients $C_{\mathbf{g}}^{(j)}$ and the normal components $\gamma^{(j)}$, which are used to obtain the scattered wave amplitudes for a given crystal thickness. The electron wave ψ at a depth z in the crystal is

$$\psi(z) = \mathcal{C}\mathcal{E}(z)\mathcal{C}^{-1}\psi_0 = \mathcal{S}(z)\psi_0 \quad (4)$$

where \mathcal{C} is the matrix containing the eigenvectors and $\mathcal{E}(z) = e^{2\pi i \gamma^{(j)} z} \delta_{ij}$ is a diagonal matrix which depends on the thickness and the Bloch wave normal components. ψ_0 is a vector containing the Fourier coefficients of the incident electron wave—in the case of plane wave illumination, it is a vector with the value of 1 at the index corresponding to the incident beam direction and zero elsewhere.

This transformation can be compactly represented by the scattering matrix \mathcal{S} which maps the vector representing the incident electron wave to the scattered wave at depth z . Writing the equation in this form, we see that the \mathcal{S} -matrix is the exponential of the structure matrix $\bar{\mathcal{A}}$ multiplied by $2\pi i z$.

2.1. Stacked \mathcal{S} -matrix model

In the description of the Bloch wave model above, we obtained a single \mathcal{S} -matrix which transformed a plane wave ψ_0 incident onto a crystal of some thickness z into the scattered wave ψ . If the electron wave were to immediately enter another crystal, we can model this further scattering by simply using the \mathcal{S} -matrix of that layer to transform the previously scattered wave into the final scattered wave [24, 32]. This operation is equivalent to multiplying the complex \mathcal{S} -matrices together and applying it once to the original wave. From a numerical standpoint, it is more convenient to successively apply the \mathcal{S} -matrices to ψ_0 rather than multiply the \mathcal{S} -matrices first, as matrix-vector multiplications are cheaper than the matrix-matrix products needed to construct the total \mathcal{S} -matrix.

In this work, we will model the trilayer STO:PTO:STO sample using the product of 3 \mathcal{S} -matrices:

$$\mathcal{S} = \mathcal{S}_{\text{STO}} \mathcal{S}_{\text{PTO}} \mathcal{S}_{\text{STO}} \quad (5)$$

For the trilayer sample we consider here, the epitaxial relationship between the layers considerably simplifies the use of the stacked \mathcal{S} -matrix approach, as the layers share the same lattice—this ensures that all of the \mathcal{S} -matrices share the same set of beams. In a situation where the layers do not share the same lattice, one must ensure that all of the component \mathcal{S} -matrices include all of the beams from all of the layers. Further, in such case it is possible for a beam scattered by the top layer to be evanescent in a lower layer, with exponentially decaying intensity [32].

2.2. Derivatives of the stacked \mathcal{S} -matrix model

Using the Bloch wave method, we have obtained a scattering matrix which is the exponential of the structure matrix, whose entries are readily obtained from the crystal properties. The full scattering matrix describing the multilayer is represented as a product of three such \mathcal{S} -matrices. In order to match the parameters of the model to our experimental data, we will use an optimization procedure to minimize the error between the model and the experiment. Unfortunately, each evaluation of the scattered wave using this model requires (for each layer) building a new \mathcal{A} -matrix and diagonalizing it, which is computationally expensive and makes numerical

optimization inefficient. Therefore we aim to obtain the derivatives of the scattering matrix with respect to the entries of the structure matrix, so that we can compute the gradient of the error without the large number of function evaluations necessitated by finite differences. Najfeld and Havel [33] define the directional derivative $D_{\mathbf{V}}(t, \mathbf{A})$ of a matrix exponential $e^{t\mathbf{A}}$ in the direction \mathbf{V} as

$$D_{\mathbf{V}}(t, \mathbf{A}) \equiv \lim_{h \rightarrow 0} \frac{1}{h} (e^{t(\mathbf{A}+h\mathbf{V})} - e^{t\mathbf{A}}) \quad (6)$$

We will also use the notation $\frac{d\mathcal{S}}{d\theta}$ to refer to the derivative of a scattering matrix in the direction \mathbf{V}_{θ} , where θ is one of the structural perturbation parameters. For a matrix which has been spectrally decomposed as $\mathbf{A} = \mathbf{U}\mathbf{\Lambda}\mathbf{U}^{-1}$, (i.e. its eigendecomposition has been computed, where the columns of \mathbf{U} contain the eigenvectors and the diagonal of $\mathbf{\Lambda}$ contains the eigenvalues λ_i) the directional derivative of its exponential can be computed as [33]

$$D_{\mathbf{V}}(t, \mathbf{A}) = \mathbf{U} ((\mathbf{U}^{-1}\mathbf{V}\mathbf{U}) \odot \mathbf{\Phi}(t)) \mathbf{U}^{-1}. \quad (7)$$

where \odot is the Hadamard, or elementwise, product. The entries of $\mathbf{\Phi}(t)$ depend on the eigenvalues of \mathbf{A} :

$$\Phi_{ij}(t) = \begin{cases} (e^{t\lambda_i} - e^{t\lambda_j})/(\lambda_i - \lambda_j) & \text{if } \lambda_i \neq \lambda_j \\ te^{t\lambda_i} & \text{if } \lambda_i = \lambda_j \end{cases} \quad (8)$$

To compute the derivative of the total \mathcal{S} -matrix comprised of an ordered collection of N separate scattering matrices indexed with the superscript (j) (i.e. $\mathcal{S} = \prod_j \mathcal{S}^{(j)}$), with respect to a parameter θ we use the product rule

$$\frac{d\mathcal{S}}{d\theta} = \sum_{i=0}^N \left[\prod_{j=0}^{j=i-1} \mathcal{S}^{(j)} \cdot \frac{d\mathcal{S}^{(i)}}{d\theta} \cdot \prod_{k=i+1}^{k=N} \mathcal{S}^{(k)} \right]. \quad (9)$$

Due to our choice of parameters for the model, many of the derivatives $\frac{d\mathcal{S}^{(j)}}{d\theta}$ will be zero. For the terms where there are nonzero derivatives, the derivative of the total \mathcal{S} -matrix comprises the scattering up to the layer affected by the parameter θ , the change in scattering within that layer, and the further scattering of the wave by the following layers in the heterostructure.

In our model of the trilayer sample, there are two relevant classes of structural perturbation that we will attempt to recover: crystal tilt and structural distortion due to polarization. In the following section, we will derive the direction matrices \mathbf{V}_{θ} for these types of perturbation.

2.2.1. Crystal tilt

Because tilt of the crystal is included solely in the diagonal elements of the structure matrix via the excitation errors $s_{\mathbf{g}}$, the derivative direction is

$$(\mathbf{V}_{\text{tilt}})_{\mathbf{g},\mathbf{h}} = 2k_0 \frac{ds_{\mathbf{g}}}{d\mathbf{k}_0} \delta_{\mathbf{g}-\mathbf{h}} \quad (10)$$

The derivative of $s_{\mathbf{g}}$ with respect to the transverse (x and y) components of the incident wavevector are approximately

$$\frac{ds_{\mathbf{g}}}{dk_{\{x,y\}}} = -\frac{g_{\{x,y\}}}{|\mathbf{g} + \mathbf{k}_0|} + \frac{(g_{\{x,y\}} + k_{\{x,y\}})(\mathbf{g} \cdot (2\mathbf{k} + \mathbf{g}))}{2|\mathbf{g} + \mathbf{k}|^3}. \quad (11)$$

We have neglected the $\cos \alpha$ term in the denominator of $s_{\mathbf{g}}$ in this derivation to greatly simplify the expression at the cost of some small error in the magnitude of $\frac{ds}{dk}$.

2.2.2. Polarization

While it is possible under certain conditions to recover the locations of each atom in the unit cell by recovering the full \mathcal{S} -matrix from diffraction data, [8, 19] here we parameterize the model in terms of the polarization directly, and displace the Ti and O sites by interpolating between their positions in the canonical non-polar and polar structures. For each atom in the unit cell, we define displacement vectors $\delta \mathbf{r}_a^{(j)}$ and $\delta \mathbf{r}_b^{(j)}$ which takes the atom from its site $\mathbf{r}^{(j)}$ in the non-polar structure to its site in the canonical polar structure, for polarizations in the a and b directions respectively. This fully polar structure for PTO is related to the nonpolar one by displacing the Pb site by 0.0281 lattice units, the $(\frac{1}{2}, 0, \frac{1}{2})$ and $(\frac{1}{2}, \frac{1}{2}, 0)$ O sites by -0.0849, and the $(0, \frac{1}{2}, \frac{1}{2})$ O site by -0.1058, while leaving the Ti sites undisturbed, in the case of a -axis polarization. For intermediate or mixed-direction polarizations, we linearly scale the displacement vectors by the relative polarization, ρ_a and ρ_b for a and b polarizations respectively. The Fourier coefficients of the crystal potential are thus written as

$$U_{\mathbf{g}} = \frac{1}{\Omega} \sum_j f_e^{(j)} e^{2\pi i((\mathbf{r}^{(j)} + \rho_a \delta \mathbf{r}_a^{(j)} + \rho_b \delta \mathbf{r}_b^{(j)}) \cdot \mathbf{g})} \quad (12)$$

where Ω is the unit cell volume, and the atomic form factors $f_e^{(j)}$ are computed using the absorptive Weickenmeier-Kohl parameterization for isolated neutral

atoms [34]. The derivative of the structure factor with respect to the relative a -axis polarization parameter, ρ_a , is then

$$\frac{dU_{\mathbf{g}}}{d\rho_a} = \frac{1}{\Omega} \sum_j 2\pi i f_e^{(j)}(\mathbf{g} \cdot \delta \mathbf{r}_a) e^{2\pi i((\mathbf{r}^{(j)} + \rho_a \delta \mathbf{r}_a^{(j)} + \rho_b \delta \mathbf{r}_b^{(j)}) \cdot \mathbf{g})} \quad (13)$$

and a similar expression arises for $\frac{dU_{\mathbf{g}}}{d\rho_b}$. The derivative direction matrix for polarization is simply filled with the derivatives of the Fourier coefficients, e.g.

$$\left(\mathbf{V}_{\rho_{\{a,b\}}} \right)_{\mathbf{g}, \mathbf{h}} = \frac{dU_{\mathbf{g}-\mathbf{h}}}{d\rho_{\{a,b\}}} \quad (14)$$

Note that we do not take into account expansion of the unit cell, so the mean inner potential term U_0 does not change, and thus polarization only affects the off-diagonal elements of the structure matrix.

2.3. Numerical Optimization

To fit the stacked \mathcal{S} -matrix model to the experimental measurements, we implemented a version of the alternating direction method of multipliers [35]. At each iteration of the optimization algorithm, we first update the model parameters at each probe position using our previously derived gradients and taking a step along the direction of steepest descent. We then perform regularization of the fitted model parameters to ensure convergence to a physically sensible solution and enforce smoothness.

2.3.1. Gradient Descent

The loss function \mathcal{L} is the sum squared difference between the simulated diffraction intensities from the model and the experimental intensities for each Bragg beam recorded

$$\mathcal{L} = \sum_{\mathbf{g}} (I_{\text{exp}}(\mathbf{g}) - \mu |\mathcal{S}\psi_0(\mathbf{g})|^2 - \nu)^2 \quad (15)$$

The modeled intensities have both an additive intensity offset ν and multiplicative scaling μ , which we found necessary in order to compensate for background noise and intensity variation in the experimental data. Note that the \mathcal{S} -matrix calculations are performed using a different, and larger, set of Bragg beams, in order to include scattering into the higher order

beams (not recorded on the detector) in the forward model. Our experimental diffraction patterns measure the intensities of 69 Bragg beams, with a maximum scattering vector of 1.1 \AA^{-1} . The \mathcal{S} -matrix calculations include 109 beams, with a maximum scattering angle of 1.5 \AA^{-1} . Only the Bragg beams present in the experiment contribute to the loss function. The derivatives of the loss function with respect to the intensity scale parameters are given as

$$\frac{\partial \mathcal{L}}{\partial \mu} = \sum_{\mathbf{g}} -2|\mathcal{S}\psi_0|^2 (I_{\text{exp}} - \mu|\mathcal{S}\psi_0|^2 - \nu) \quad (16)$$

$$\frac{\partial \mathcal{L}}{\partial \nu} = \sum_{\mathbf{g}} -2 (I_{\text{exp}} - \mu|\mathcal{S}\psi_0|^2 - \nu) \quad (17)$$

(where we have dropped the dependence on \mathbf{g} from the notation for compactness). The derivatives with respect to the structure perturbations involve the derivatives of the \mathcal{S} -matrix, and so are much more complicated expressions. For a generic parameter θ that enters into the \mathcal{S} -matrices, the derivative of the loss function is

$$\frac{\partial \mathcal{L}}{\partial \theta} = -4\mu \Re \left[\psi^* \frac{d\mathcal{S}}{d\theta} \psi_0 \right] \cdot [I_{\text{exp}} - \mu|\mathcal{S}\psi_0|^2 - \nu] \quad (18)$$

The gradients with respect to the tilt and polarization variables are obtained using the derivative directions in Eqs. 11 and 13, the product rule in Eq. 9, and the \mathcal{S} -matrix derivative method in Eq. 7. At each step of the optimization procedure, we update the parameters by taking a step along the negative gradient direction of this loss function. In some previous works, such as those based on quantitative CBED [36], optimization would begin by first refining the geometrical factors in the model such as tilt and thickness before proceeding to refine structural distortions such as polarization. In this work, we instead begin updating all parameters from the start of iteration but use regularization in order to rapidly and robustly converge on a solution.

2.3.2. Regularization

In order to obtain physically sensible solutions to the optimization problem we found it necessary to apply several regularizers. Before performing the optimization, we de-noise the integrated disk intensities using principal component analysis, retaining the first 16 components.

At each iteration step, we apply further regularization. First, the estimated parameters are smoothed across the real-space dimensions of the scan using a Gaussian kernel. Since the intensity scale and offset and the tilts are expected to vary slowly across the field of view, we used a kernel size of 50 nm for the intensity parameters and 25 nm for the tilts. The polarization is expected to vary more rapidly, so we used a kernel size of 2 nm. Note that the experiment used a probe step size of 1 nm, giving equivalent values for the size of each kernel in terms of the number of probe positions.

In addition, we also clip the fitted parameters to be within set bounds, so that outliers do not excessively propagate error to their neighbors via the smoothing kernel. We note that we do not apply any explicit high-pass filtering to the fitted polarization values (on the contrary, they are Gaussian filtered, albeit with a very small kernel size). However, the strong smoothing regularization applied to the tilt and intensity signals can have the side effect of forcing all of the high frequency variation into the polarization channel.

2.4. Atomic Form Factors

Wu et al [37] showed that 4D-STEM may be sensitive to the charge transfer between sites in ionic materials, using strontium titanate as a model system, which would imply that the independent atom model for the crystal potential may not be valid for our computations. To test this possibility we used the GPAW density functional theory package [38] to simulate the charge transfer between species, and then used abTEM [39] to perform diffraction simulations for the simulated charge densities that match our experimental conditions. From these simulations we observed that the maximum deviation in the diffracted intensities between the DFT and IAM potentials was approximately 0.1% of the probe intensity, validating the use of the IAM model for our computations.

3. Methods

3.1. Heterostructure Growth

We synthesized a trilayer structure consisting of 16 unit cells of SrTiO_3 , 16 unit cells of PbTiO_3 , and 16 unit cells of SrTiO_3 , on top of a SrRuO_3 buffer layer on a single crystal DyScO_3 substrate, giving a total heterostructure

thickness of ≈ 19 nm. The layers were grown at 610°C in a 100 mTorr oxygen atmosphere, using reflection high-energy electron diffraction (RHEED)-assisted pulsed laser deposition (PLD) with a KrF laser. The trilayer structure was prepared for TEM analysis by mechanical polishing followed by ion milling. Within the imaged area the substrate has been completely removed, leaving only the heterostructure.

3.2. 4D-STEM Experiments

We performed 4D-STEM measurements on the TEAM I microscope, an aberration-corrected Thermo Fisher Scientific Titan operated at 300 kV with a probe current of 100 pA. We used a STEM probe semiangle of 2 mrad, and a STEM probe step size of 1 nm. We recorded zero-loss filtered diffraction patterns using a Gatan K3 direct electron detector located beyond a Gatan Continuum energy filter. We operated the K3 detector in electron counting mode using a binning of 4x4 pixels, a camera length of 1.05 m, and an exposure time of 47 ms. We analyzed the 4D-STEM experiments using custom Python and Matlab code. The diffraction pattern simulations and Bloch wave calculations and optimizations have been implemented as part of the py4DSTEM analysis toolkit [40–42]. Initial processing of the data was performed by selecting the 69 Bragg disks visible on the detector and integrating their intensities. All further analysis was conducted using these integrated disk intensities rather than the pixelwise intensity of the recorded patterns. As a result, the analysis is not expected to be sensitive to distortion by the post-specimen optics or the point-spread function of the detector.

4. Results & Discussion

4.1. Tilt/Polarization Confounding

Figure 2 shows how local mistilts of the sample from the perfect zone axis orientation can confound the measurement of local polarization when using a conventional metric based on Friedel pair asymmetry. The top row of Fig. 2a shows a sequence of simulated diffraction patterns for the STO/PTO trilayer sample at varying polarization in the x -direction. The inset numbers indicate the polarization signal measured using the anomalous contrast of the (200) Friedel pair [16], computed as

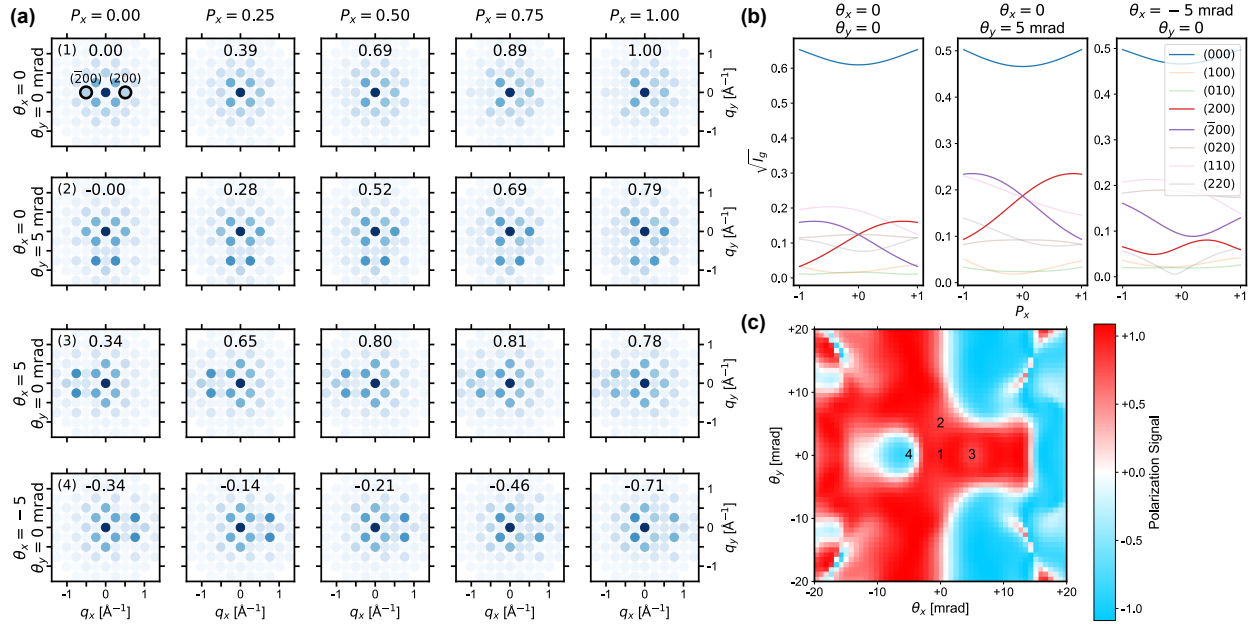


Figure 2: Confounding of tilt and polarization signals for a STO:PTO:STO trilayer. (a) Sequences of diffraction patterns simulated at relative x -direction polarization varying from 0–1 for various mistilts from a perfect $[001]$ orientation. The two diffraction disks conventionally used to measure polarization, (200) and $(\bar{2}00)$ are highlighted, and the inset text indicates the relative polarization measured as $\frac{I_{200} - I_{\bar{2}00}}{I_{200} + I_{\bar{2}00}}$. (b) Line traces of selected diffraction intensities for different mistilts, with the (200) and $(\bar{2}00)$ reflections highlighted. (c) Map of apparent polarization signal for a trilayer with $P_x = 1$ as measured from the asymmetry of the (200) and $(\bar{2}00)$ disks for different mistilts. Contrast reversals in the polarization signal occur with at little as 5 mrad mistilt. The overlaid numbers indicate the tilt values corresponding to the rows of (a).

$(I_{200} - I_{\bar{2}00})/(I_{200} + I_{\bar{2}00})$ and normalized to the $\theta_x = \theta_y = 0$, $P_x = 1$ value. The signal is monotonic with increasing polarization and approximately linear, indicating that in the ideal case the symmetry breaking of this pair of diffraction disks is a good measurement of the local polarization. As shown in the left panel of Fig. 2b, the intensities of these disks branch as a function of polarization. When tilting the incident beam towards the positive y -axis, as in the second row of Fig. 2a, the symmetry of (200) pair of diffraction disks is not broken, but the different excitation of these beams (shown in the center panel of Fig. 2b) causes the signal to be suppressed by approximately 20%. However, when the beam is tilted by 5 mrad ($\approx 0.3^\circ$) towards the x -axis (as shown in the right panel of Fig. 2b), the effect of the tilting is to break the symmetry of the (200) disks. This slight mistilt in either direction along the x -axis completely destroys the polarization measurement. In the third row of Fig. 2a, where the beam is tilted towards the positive x -axis, there is an apparent nonzero polarization even when the material is not polarized. In the fourth row of Fig. 2a (and the right panel of Fig. 2b) a tilt towards the negative x -axis causes an inversion of the polarization signal when $P_x > 0$, non-monotonic behavior when $P_x < 0$, as well as an apparent nonzero polarization even when the material is not polarized. These effects are plotted as a function of x and y tilts in Fig. 2c.

4.2. Gradients of the Diffracted Intensities

Computations of the derivatives of the diffraction disk intensities with respect to x -direction polarization and tilt are shown in Figure 3, evaluated over a range of tilts and polarizations. The inset numbers indicate the difference between the derivative of the (200) Friedel pair, which demonstrates the sensitivity of the signal derived from the anomalous contrast of those reflections to the chosen parameter. The difference in overall magnitude between the polarization and tilt derivatives is affected by the choice of units for the parameters; in the figure they have been scaled to be visually uniform, and in the optimization procedure the problem is rescaled to promote uniform convergence along all the parameter directions. In the on-zone, unpolarized case ($P = 0$, $\theta = 0$) in the top left, the (200) anomalous contrast signal will not distinguish between polarization of the crystal and tilt, as both cause the same anomalous contrast. However, other reflections respond in different ways to polarization and tilt. Thus, when considering all of the diffracted beams the

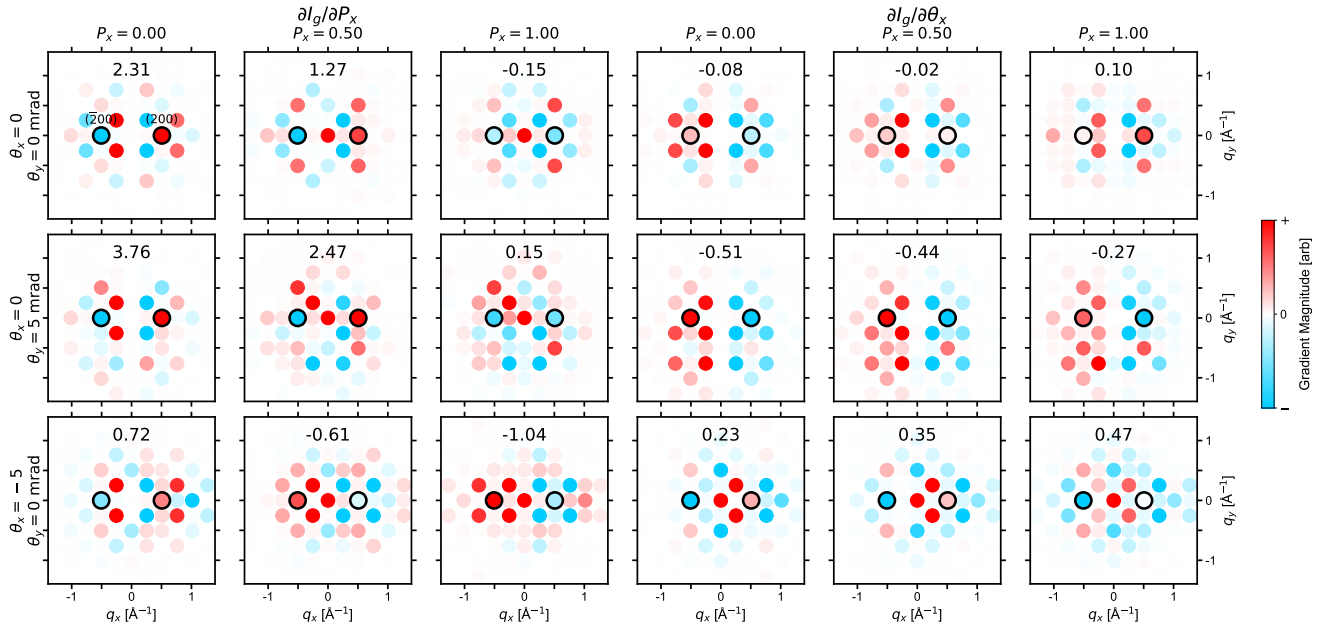


Figure 3: Derivatives of the diffracted intensities with respect to x -polarization P_x and tilt about the x -axis θ_x . The inset numbers show the value of $\frac{\partial I_{200}}{\partial \vartheta} - \frac{\partial I_{\bar{2}00}}{\partial \vartheta}$ in arbitrary units, where ϑ represents polarization for the left 3 columns, and tilt for the right 3 columns.

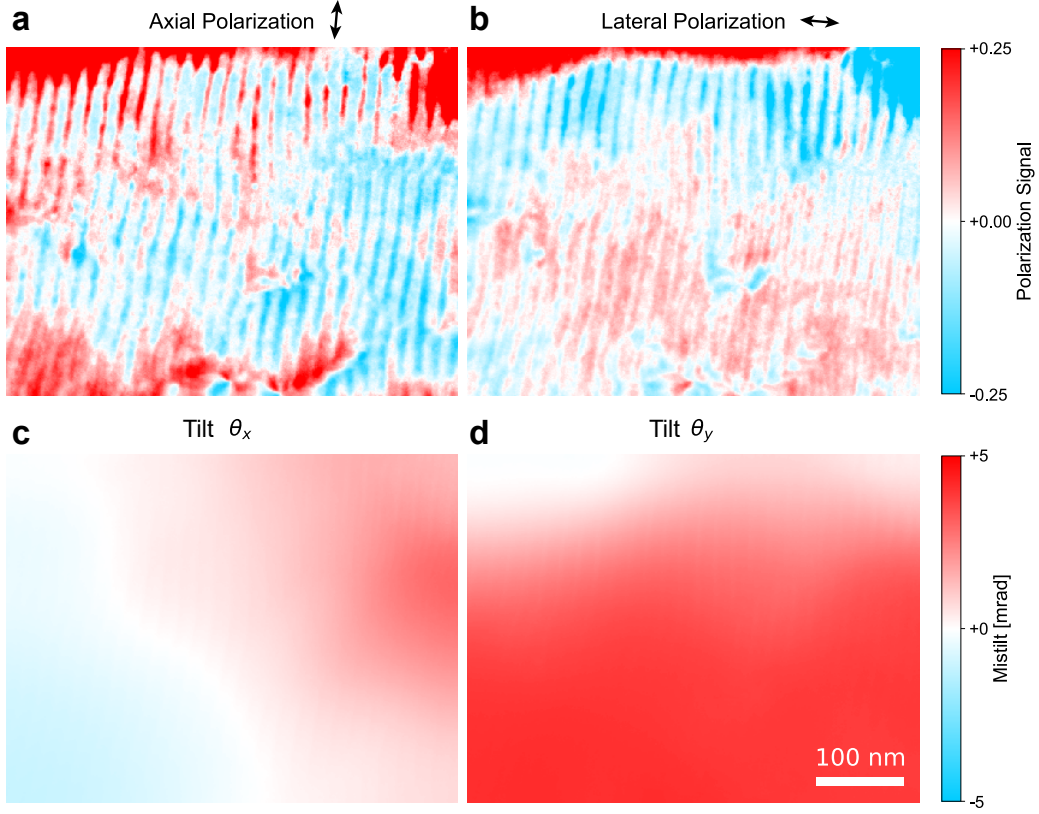


Figure 4: (a),(b) Polarization and (c),(d) tilt of the STO:PTO:STO sample recovered from experimental measurements using the optimization procedure. Approximate polarization directions are labeled above.

gradient directions for tilt and polarization are approximately 62° separated. Since they are not orthogonal, an iterative optimization will be needed in order to solve the polarization and tilt. In the case of nonzero polarization and tilt, the gradients tend to become more parallel. In particular the gradients with respect to y -direction polarization and tilt, which are fully orthogonal to the x -direction parameter gradients at $P = 0$, $\theta = 0$, will become partially coupled to the other direction when the crystal is tilted or polarized.

4.3. Experimental Results

The fitted polarization and tilts of the STO:PTO:STO multilayer sample are plotted in Fig. 4 over the full field of view. Immediately, we can see several domains in the polarization maps in Figs. 4a and b where the regular periodic structures show the tubular vortex structures. The “axial” polarization represents the PTO polarization along the directions parallel to the vortex cores, while the “lateral” polarization is perpendicular. Inside each vortex, the projected polarization is relatively constant in a given domain. Various domain boundaries are also visible, where the polarization abruptly changes sign, in either the axial or lateral directions, or both. These domain structures and domain walls are in good agreement with previous observations of STO/PTO multilayer samples [15, 29, 43]. The tilt maps shown in Figs. 4c and d show significant rotation from the ideal zone axis, especially in the y -axis direction. These maps demonstrate the need to include tilt in the modeling of the diffraction signals. The smoothness of the estimated tilt is due in part to the strong regularization applied during the reconstruction.

The polarization maps contain many complex domain and domain wall structures. We expect that the vortex cores will have alternating polarization signs in the axial direction. This alternating structure is visible in all domains in Fig. 4a, though interestingly we also observe a negative offset from zero mean axial polarization in the largest domain spanning the grain in the bottom half of the map. The grains at the top and bottom edges also show a significant positive offset from zero mean. These observations suggest that there may be a net axial polarization in many of the domains, which can’t be directly observed from qualitative estimates of the polarization which have been high-pass filtered [43].

By contrast, in the lateral direction we expect oscillations in the polarization, but that each domain will have a larger net positive or negative polarization. This is because phase field predictions of the polarization structure of the PTO vortex phase predict that that every other vortex will be displaced towards one of the STO/PTO interfaces, while the remaining vortices will be displaced towards the other PTO/STO interface [43]. This in turn causes a net polarization flow to one of the lateral directions. Susarla et al. provide more phase field modeling and predicted vortex domain structures [43]. These net polarization features are

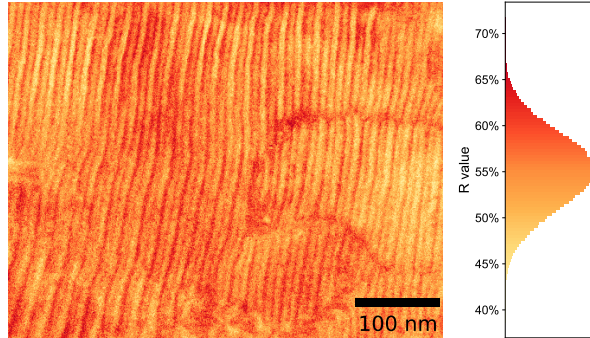


Figure 5: R value of the fitted model at each scan position.

indeed observed in Fig. 4b, and the overall magnitude of the measured polarization is similar to those observed previously. Domains in the top third of the map and bottom left show significant polarization towards the negative direction, while the domains in the bottom two thirds show significant polarization in the positive direction. Various small domains are interspersed into the larger domains, but each shows a non-zero mean polarization. Overall, these observations provide a significant step forward in accurate modeling of the intensity of Bragg peaks when the beam undergoes significant multiple scattering and the sample has a large mistilt from the ideal zone axis.

The goodness of fit of the model is plotted for each scan position in Fig. 5, using the residue, or R -value, defined as

$$R = \frac{\sum_{\mathbf{g}} |I_{\text{exp}}(\mathbf{g}) - \mu|\mathcal{S}\psi_0(\mathbf{g})|^2|}{\sum_{\mathbf{g}} I_{\text{exp}}(\mathbf{g})} \quad (19)$$

Overall the R values are relatively high, with an average of about 55%, though they are consistent across the field of view. The overall high value of this residue may point to a systematic mismatch between the experiment and the model. Surface contamination, a small amount of remaining buffer layer from the synthesis procedure, or the presence of an amorphous damage layer could all contribute to another source of diffracted intensity that cannot be accounted for by the model. Incorrect estimates of the Debye-Waller factors also change the distribution of intensity between the different orders of diffraction, leading to high residue values but not

preventing the local parameter variations from being recovered well. The application of strong regularization on the recovered parameters is also likely to lead to larger residue values. A better fit could be achieved by tuning global parameters such as the Debye-Waller factors, regularization strength, or weighting of intensities in the loss function, though this would add considerably to the computational complexity. Recent advances in interpretable machine learning may offer an efficient means for tuning these hyperparameters, in particular the methods known as “algorithm unrolling,” which provides a connection between iterative algorithms like the one we use here, and deep learning frameworks [44]. In addition, there is finer variation in the residue which corresponds to the fluctuations in polarization. As we discuss in the following section, the structure of the polarization in this sample is more complex than the model we have used can capture, as it varies along the beam direction as well as in-plane.

4.4. Future Directions

In this work we have shown a stacked \mathcal{S} -matrix model for scattering through a trilayer heterostructure parameterized with a single homogeneous polarization direction within the PTO layer. However, the samples we investigated are known to have polarization that varies in a complex manner through the thickness. A natural extension of Equation 5 to account for this is to model the PTO layer with a product of N_L \mathcal{S} -matrices with distinct polarization:

$$\mathcal{S}_{\text{PTO}} = \prod_i^{N_L} \hat{\mathcal{S}}_{\text{PTO}}(\rho_{a,i}, \rho_{b,i}; t = T/N_L) \quad (20)$$

where $\rho_{a,i}$ and $\rho_{b,i}$ are the relative polarization of the i -th layer in the a and b directions, and T is the total thickness. This modification to the model allows us to more accurately reproduce the physics of the scattering, at the cost of adding substantially more optimization variables. This added complexity can be mitigated somewhat by applying constraints to the variation in polarization with thickness. For example, if the polarization is constrained to vary linearly then the polarization variables at the i -th layer are expressed in terms of just two optimization variables, ρ_{top} and ρ_{bottom} regardless of the number of layers modeled

$$\rho_i = \rho_{\text{top}} + \frac{i}{N_L - 1}(\rho_{\text{bottom}} - \rho_{\text{top}}) \quad (21)$$

Pennington and Koch [26] have used a similar stacked model to solve for polarization changes along the beam direction, but their approach relies on having a “composite” CBED measurement that spans a large range of incident beam directions. This approach is both experimentally more challenging and several orders of magnitude more computationally intensive, but the inclusion of many beam directions may be necessary in order to obtain 3D information. It may also be possible to use multibeam electron diffraction [45] to obtain several nanobeam diffraction patterns with large angular separation simultaneously.

5. Conclusions

In this work, we have constructed a model of the electron multiple scattering through a complex multi-layer sample, parameterized over the physically relevant variables, and utilized an optimization procedure to fit the model to experimental data. Simple models for measuring the polarization of materials from nanobeam electron diffraction patterns, using symmetry breaking of pairs of diffracted disks, break down in the presence of even small tilts of the crystal, causing contrast changes and reversals. Using a stacked \mathcal{S} -matrix approach, we are able to use all of the scattered beams to determine polarization and tilt simultaneously. In order to make the problem computationally feasible for a large area scan, we derived the analytic gradients of the diffraction intensities and used them to perform regularized gradient descent.

6. Acknowledgements

SEZ and CO thank Alireza Sadri for reference to the literature on matrix exponential derivatives, Scott Findlay for suggesting the gradient approach and proofreading the manuscript, Toma Susi for useful discussions regarding the use of density functional theory in diffraction simulations, and Christoph Koch for discussions on the stacked Bloch wave approach. SEZ was supported by the National Science Foundation under STROBE Grant No. DMR 1548924. HGB acknowledges the support of a University of Melbourne early career researcher award. CO acknowledges support of a US Department of Energy Early Career Research Award. Work at the

Molecular Foundry was supported by the Office of Science, Office of Basic Energy Sciences, of the U.S. Department of Energy under Contract No. DE-AC02-05CH11231.

References

- [1] H. Yang, I. MacLaren, L. Jones, G. T. Martinez, M. Simson, M. Huth, H. Ryll, H. Soltau, R. Sagawa, Y. Kondo, et al., Electron ptychographic phase imaging of light elements in crystalline materials using wigner distribution deconvolution, *Ultramicroscopy* 180 (2017) 173–179.
- [2] T. Seki, K. Khare, Y. O. Murakami, S. Toyama, G. Sánchez-Santolino, H. Sasaki, S. D. Findlay, T. C. Petersen, Y. Ikuhara, N. Shibata, Linear imaging theory for differential phase contrast and other phase imaging modes in scanning transmission electron microscopy, *Ultramicroscopy* 240 (2022) 113580.
- [3] C. Mahr, K. Müller-Caspary, T. Grieb, M. Schowalter, T. Mehrtens, F. F. Krause, D. Zillmann, A. Rosenauer, Theoretical study of precision and accuracy of strain analysis by nano-beam electron diffraction, *Ultramicroscopy* 158 (2015) 38–48.
- [4] D. Cooper, T. Denneulin, N. Bernier, A. Béch , J.-L. Rouvi re, Strain mapping of semiconductor specimens with nm-scale resolution in a transmission electron microscope, *Micron* 80 (2016) 145–165.
- [5] T. C. Pekin, C. Gammer, J. Ciston, A. M. Minor, C. Ophus, Optimizing disk registration algorithms for nanobeam electron diffraction strain mapping, *Ultramicroscopy* 176 (2017) 170–176.
- [6] S. E. Zeltmann, A. M ller, K. C. Bustillo, B. Savitzky, L. Hughes, A. M. Minor, C. Ophus, Patterned probes for high precision 4D-STEM Bragg measurements, *Ultramicroscopy* 209 (2020) 112890.
- [7] Z. Chen, Y. Jiang, Y.-T. Shao, M. E. Holtz, M. Odstr il, M. Guizar-Sicairos, I. Hanke, S. Ganschow, D. G. Schlom, D. A. Muller, Electron ptychography achieves atomic-resolution limits set by lattice vibrations, *Science* 372 (2021) 826–831.

- [8] J. J. Donatelli, J. C. H. Spence, Inversion of many-beam Bragg intensities for phasing by iterated projections: Removal of multiple scattering artifacts from diffraction data, *Phys. Rev. Lett.* 125 (2020) 065502.
- [9] J. C. Spence, J. Zuo, M. O’Keeffe, K. Marthinsen, R. Hoier, On the minimum number of beams needed to distinguish enantiomorphs in x-ray and electron diffraction, *Acta Crystallographica Section A: Foundations of Crystallography* 50 (1994) 647–650.
- [10] J. Spence, Direct inversion of dynamical electron diffraction patterns to structure factors, *Acta Crystallographica Section A* 54 (1998) 7–18.
- [11] U. Weierstall, Q. Chen, J. Spence, M. Howells, M. Isaacson, R. Panepucci, Image reconstruction from electron and x-ray diffraction patterns using iterative algorithms: experiment and simulation, *Ultramicroscopy* 90 (2002) 171–195.
- [12] K. Müller, A. Rosenauer, M. Schowalter, J. Zweck, R. Fritz, K. Volz, Strain measurement in semiconductor heterostructures by scanning transmission electron microscopy, *Microscopy and Microanalysis* 18 (2012) 995–1009.
- [13] L. Clark, H. Brown, D. Paganin, M. Morgan, T. Matsumoto, N. Shibata, T. Petersen, S. Findlay, Probing the limits of the rigid-intensity-shift model in differential-phase-contrast scanning transmission electron microscopy, *Physical Review A* 97 (2018) 043843.
- [14] M. C. Cao, Y. Han, Z. Chen, Y. Jiang, K. X. Nguyen, E. Turgut, G. D. Fuchs, D. A. Muller, Theory and practice of electron diffraction from single atoms and extended objects using an empad, *Microscopy* 67 (2018) i150–i161.
- [15] S. Das, Y. Tang, Z. Hong, M. Gonçalves, M. McCarter, C. Klewe, K. Nguyen, F. Gómez-Ortiz, P. Shafer, E. Arenholz, et al., Observation of room-temperature polar skyrmions, *Nature* 568 (2019) 368–372.
- [16] P. Deb, M. C. Cao, Y. Han, M. E. Holtz, S. Xie, J. Park, R. Hovden, D. A. Muller, Imaging polarity in two dimensional materials by breaking friedel’s law, *Ultramicroscopy* 215 (2020) 113019.

- [17] C. Mahr, T. Grieb, F. F. Krause, M. Schowalter, A. Rosenauer, Towards the interpretation of a shift of the central beam in nano-beam electron diffraction as a change in mean inner potential, *Ultramicroscopy* 236 (2022) 113503.
- [18] K. X. Nguyen, Y. Jiang, M. C. Cao, P. Purohit, A. K. Yadav, P. García-Fernández, M. W. Tate, C. S. Chang, P. Aguado-Puente, J. Íñiguez, et al., Transferring orbital angular momentum to an electron beam reveals toroidal and chiral order, *arXiv preprint arXiv:2012.04134* (2020).
- [19] H. G. Brown, Z. Chen, M. Weyland, C. Ophus, J. Ciston, L. J. Allen, S. D. Findlay, Structure retrieval at atomic resolution in the presence of multiple scattering of the electron probe, *Physical Review Letters* 121 (2018) 266102.
- [20] P. M. Pelz, H. G. Brown, S. Stonemeyer, S. D. Findlay, A. Zettl, P. Ercius, Y. Zhang, J. Ciston, M. Scott, C. Ophus, Phase-contrast imaging of multiply-scattering extended objects at atomic resolution by reconstruction of the scattering matrix, *Physical Review Research* 3 (2021) 023159.
- [21] S. D. Findlay, H. G. Brown, P. M. Pelz, C. Ophus, J. Ciston, L. J. Allen, Scattering matrix determination in crystalline materials from 4D scanning transmission electron microscopy at a single defocus value, *Microscopy and Microanalysis* 27 (2021) 744–757.
- [22] H. G. Brown, P. M. Pelz, S.-L. Hsu, Z. Zhang, R. Ramesh, K. Inzani, E. Sheridan, S. M. Griffin, M. Schloz, T. C. Pekin, et al., A three-dimensional reconstruction algorithm for scanning transmission electron microscopy data from a single sample orientation, *Microscopy and Microanalysis* 28 (2022) 1632–1640.
- [23] L. Sturkey, The calculation of electron diffraction intensities, *Proceedings of the Physical Society* (1958-1967) 80 (1962) 321.
- [24] R. S. Pennington, W. Van den Broek, C. T. Koch, Third-dimension information retrieval from a single convergent-beam transmission electron diffraction pattern using an artificial neural network, *Phys. Rev. B* 89 (2014) 205409.

- [25] R. S. Pennington, C. T. Koch, Retrieving depth-direction information from TEM diffraction data under reciprocal-space sampling variation, *Ultramicroscopy* 148 (2015) 105–114.
- [26] R. S. Pennington, C. T. Koch, A three-dimensional polarization domain retrieval method from electron diffraction data, *Ultramicroscopy* 155 (2015) 42–48.
- [27] R. S. Pennington, C. Coll, S. Estradé, F. Peiró, C. T. Koch, Neural-network-based depth-resolved multiscale structural optimization using density functional theory and electron diffraction data, *Phys. Rev. B* 97 (2018) 024112.
- [28] D. Jacob, J. Zuo, A. Lefebvre, Y. Cordier, Composition analysis of semiconductor quantum wells by energy filtered convergent-beam electron diffraction, *Ultramicroscopy* 108 (2008) 358–366.
- [29] A. Yadav, C. Nelson, S. Hsu, Z. Hong, J. Clarkson, C. Schlepütz, A. Damodaran, P. Shafer, E. Arenholz, L. Dedon, et al., Observation of polar vortices in oxide superlattices, *Nature* 530 (2016) 198–201.
- [30] Z. Shao, N. Schnitzer, J. Ruf, O. Y. Gorobtsov, C. Dai, B. H. Goodge, T. Yang, H. Nair, V. A. Stoica, J. W. Freeland, J. Ruff, L.-Q. Chen, D. G. Schlom, K. M. Shen, L. F. Kourkoutis, A. Singer, Real-space imaging of polar and elastic nano-textures in thin films via inversion of diffraction data, 2022.
- [31] M. De Graef, Introduction to conventional transmission electron microscopy, Cambridge university press, 2003.
- [32] S. Singh, M. Mills, M. D. Graef, Dynamical scattering image simulations for two-phase γ - γ' microstructures: A theoretical model, *Ultramicroscopy* 185 (2018) 32–41.
- [33] I. Najfeld, T. Havel, Derivatives of the matrix exponential and their computation, *Advances in Applied Mathematics* 16 (1995) 321–375.
- [34] A. Weickenmeier, H. Kohl, Computation of absorptive form factors for high-energy electron diffraction, *Acta Crystallographica Section A: Foundations of Crystallography* 47 (1991) 590–597.

- [35] S. Boyd, N. Parikh, E. Chu, B. Peleato, J. Eckstein, et al., Distributed optimization and statistical learning via the alternating direction method of multipliers, *Foundations and Trends in Machine learning* 3 (2011) 1–122.
- [36] Z. JM, Quantitative convergent beam electron diffraction, *Materials Transactions, JIM* 39 (1998) 938–946.
- [37] L. Wu, Q. Meng, Y. Zhu, Mapping valence electron distributions with multipole density formalism using 4D-STEM, *Ultramicroscopy* 219 (2020) 113095.
- [38] J. J. Mortensen, L. B. Hansen, K. W. Jacobsen, Real-space grid implementation of the projector augmented wave method, *Phys. Rev. B* 71 (2005) 035109.
- [39] J. Madsen, T. Susi, The abTEM code: transmission electron microscopy from first principles [version 2; peer review: 2 approved], *Open Research Europe* 1 (2021).
- [40] B. H. Savitzky, S. E. Zeltmann, L. A. Hughes, H. G. Brown, S. Zhao, P. M. Pelz, T. C. Pekin, E. S. Barnard, J. Donohue, L. R. DaCosta, et al., py4DSTEM: A software package for four-dimensional scanning transmission electron microscopy data analysis, *Microscopy and Microanalysis* 27 (2021) 712–743.
- [41] C. Ophus, S. E. Zeltmann, A. Bruefach, A. Rakowski, B. H. Savitzky, A. M. Minor, M. C. Scott, Automated crystal orientation mapping in py4dstem using sparse correlation matching, *Microscopy and Microanalysis* 28 (2022) 390–403.
- [42] S. E. Zeltmann, A. M. Minor, C. Ophus, 4D-STEM measurement of thickness and orientation by Bloch wave dynamical diffraction matching, *Microscopy and Microanalysis* 28 (2022) 382–383.
- [43] S. Susarla, S. Hsu, F. Gómez-Ortiz, B. Savitzky, S. Das, P. Behera, J. Junquera, P. Ercius, R. Ramesh, C. Ophus, The emergence of three-dimensional chiral domain walls in polar vortices, *Manuscript under review* (2022).

- [44] V. Monga, Y. Li, Y. C. Eldar, Algorithm unrolling: Interpretable, efficient deep learning for signal and image processing, *IEEE Signal Processing Magazine* 38 (2021) 18–44.
- [45] X. Hong, S. E. Zeltmann, B. H. Savitzky, L. R. DaCosta, A. Müller, A. M. Minor, K. C. Bustillo, C. Ophus, Multibeam electron diffraction, *Microscopy and Microanalysis* 27 (2021) 129–139.